J. Biomechanics, 1974, Vol. 7, pp. 277–285. Pergamon Press. Printed in Great Britain

FINITE ELEMENT STRESS ANALYSIS OF AN INTERVERTEBRAL DISC*

T. BELYTSCHKO, R. F. KULAK, A. B. SCHULTZ

Department of Materials Engineering, University of Illinois at Chicago Circle, Chicago, Illinois 60680, U.S.A.

and

J. O. GALANTE

Department of Orthopaedic Surgery, Rush-Presbyterian St. Lukes, Chicago, Illinois, U.S.A.

Abstract—An axisymmetric finite element model is employed for the study of the behavior of an intervertebral disc under axial loading. By matching experimental results on the overall behavior of the disc, orthotropic linear material constants are obtained for the annulus fibrosis for various load levels. Results are then presented on the effects of material properties and geometry on the stress-distribution and intradiscal pressures. It is shown that: (1) an adequate representation of disc behavior requires the inclusion of material anisotropy; (2) material properties of the annulus obtained by direct measurement underestimate the stiffness of the material; (3) reasonable predictions of variations of disc stiffness with vertebral level can be made on the basis of geometry; and (4) degenerative changes associated with loss of elasticity have little effect on the intradiscal pressure, while annular tears result in reduced pressure in agreement with clinical observations.

INTRODUCTION

An understanding of the mechanics of the intervertebral disc is pertinent to numerous medical problems. Among these are the pathogenesis of disc degeneration, effects of vertebral arthrodesis, endplate fractures during pilot ejections, disc replacement, and the development and correction of spinal deformities. However, at the present time, even some of the salient features of the disc's mechanical behavior are poorly understood. This is a consequence of the difficulties of (1) determining *in vivo* mechanical properties and (2) constructing a realistic analytical model.

Overall static force deflection properties of the intervertebral disc have been measured by Rolander (1966), Nachemson (1960), Brown *et al.* (1957) and Markolf (1971, 1972) among others. Tensile properties of the annulus fibrosis, a component of the disc, have been measured by Galante (1967). A complete characterization of the material properties of the annulus fibrosis is however an almost insurmountable task, for it is orthotropic and hence at least seven distinct material constants must be determined for a linear analysis. Determination of these constants is difficult even for inert materials.

One of the first semi-analytical models of the disc was developed by Sonnerup (1972). For purposes of tractability, the model neglected axial variations of stresses and material orthotropy. However, with the advent of computer methods of stress analysis, particularly finite element methods, the development of realistic models has become possible. Finite element methods have been used by Wiederhielm *et al.* (1968) for the structural response of arterioles and Kobayashi *et al.* (1971) for the stress analysis of the corneo–scleral shell.

In this report, a finite element model of the intervertebral disc is presented. Two investigations were carried out using the model: (1) determination of material constants by comparison with experimental results for the overall behavior of the disc; and (2) a study of the stress distributions, deflections and stiffnesses of discs under axial loads, and how they are influenced by disc geometry and material properties.

ANATOMY

The human vertebral column is a segmented structure consisting of 24 mobile vertebrae separated by intervertebral discs. The intervertebral disc consists of three parts: the annulus fibrosis in the periphery, the cartilage plates above and below, and the nucleus pulposus in the center.

The annulus fibrosis (see Fig. 1) in the adult lumbar spine is formed by a series of concentric encircling lamellae (Fick, 1904; Beadle, 1931). The lamellae consist of collagen fibers which have two well defined axes of orientation. In the lumbar spine, the fibers in each lamella run in a single direction, alternating

* *Received* 20 *June* 1973.

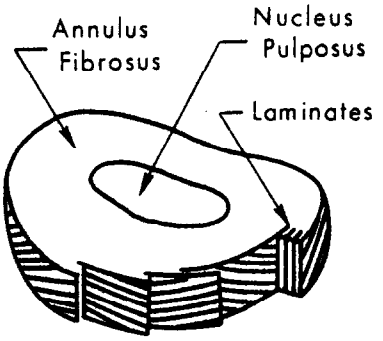

Fig. 1. The invertebral disc.

from the previous one and aligned at an angle of 30° with the horizontal axis according to Rouviere (1921) or at an angle between 24° and 37°, according to Horton (1958).

The nucleus pulposus is located nearly in the center of the disc; it is bounded above and below by the superior and inferior cartilagenous end-plates and on its periphery by the annulus fibrosis. It is composed of non-orientated collagen fibrils enmeshed in a mucoprotein gel. The water content of the nucleus ranges from 88 per cent at birth to approximately 69 per cent at the age of 77. Nachemson (1960) reported hydrostatic behavior of the nucleus in normal discs. In degenerated discs he found that the pressures are usually lower than in normal discs. Exterior to the disc proper are two ligaments: the anterior longitudinal ligament and the posterior longitudinal ligament. The anterior ligament is attached to the disc ventrally while the posterior ligament is attached dorsally.

Each vertebra consists of a body and a set of posterior elements. The center of the vertebral body is composed of soft bone and is encased circumferentially by a thin shell of cortical (compact) bone. The upper and lower surfaces of the body—which are also thin plates of cortical bone—constitute the bony end plates. During axial loading the intervertebral disc appears to be the primary load-carrying structure between vertebrae (Rolander, 1966; Hirsch and Nachemson, 1954).

FINITE ELEMENT MODEL

The anterior components of a disc unit (the intervertebral disc and adjacent vertebral bodies) are idealized as a three dimensional structure that is rotationally symmetric with respect to the vertical centerline. Based upon the assumption that little if any load is transmitted outside the body of the vertebrae during small axial deformations, only the body is modeled. The anterior and posterior longitudinal ligaments are not included in this model. Two adjacent vertebrae and their intervertebral discs are assumed to be symmetric about their horizontal center-planes. In view of these symmetries, the finite element model shown in Fig. 2 is sufficient.

Two mesh sizes were used: a fine and a coarse. The fine mesh model is divided into six distinct regions (Fig. 2). The vertebral core (soft bone), represented by region 1 in Fig. 2, is assumed to be an isotropic, homogeneous material with a mean modulus of elasticity equal to 7·5 kp/mm^2 (Yamada, 1970). The thin outer shell and the bony end plate, regions 2 and 3 respectively, are also isotropic and homogeneous with a Young's modulus of 1·61 × 10^3 kp/mm^2 (Evans, 1970). A Poisson's ratio of 0·25 is assumed for both soft and hard bone. The nucleus pulposus, region 4, in accordance with experimental results previously cited, is assumed to be incompressible and in a hydrostatic state of stress.

The annulus fibrosis corresponds to region 5, which is further sub-divided to account for the inhomogeneity of the annulus. Since the lamellae are of microscopic thickness, there are many in each subregion, so the lamellae are modeled as a single homogeneous orthotropic material with properties obtained by averaging the properties of the individual lamellae. The annulus inhomogeneity is taken into account by varying Young's modulus in the fiber direction, $E_L(r)$.

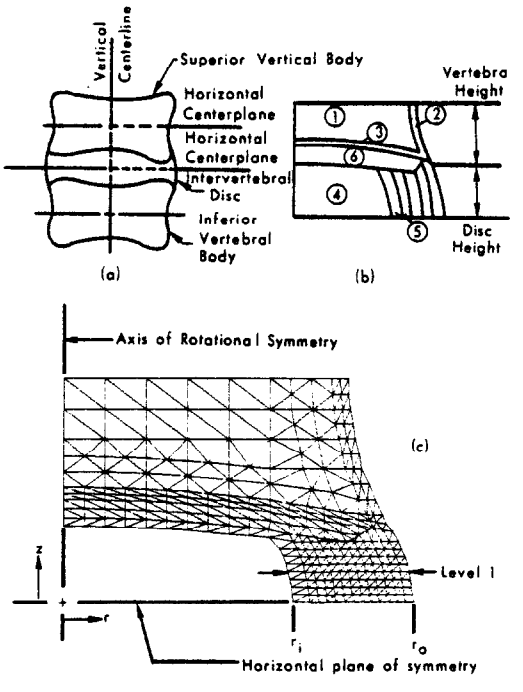

Fig. 2. Finite element model of the disc.

according to the relation Sonnerup obtained on the basis of Galante's experimental results:

$$E_L(r) = \frac{0{\cdot}3\,E_L(r_0)}{1 - 0{\cdot}7\,r/r_0} \tag{1}$$

where r is the radial coordinate and r_0 is the outer radius of the disc. The cartilagenous end plate, region 6, is regarded as an isotropic, homogeneous material with a modulus equal to 2·43 kp/mm^2 (Yamada) and a Poisson's ratio of 0·4.

The fine mesh is sized according to Rolander's (1966) specimen number 37; it is an L2-L3 lumbar disc with a height of 12 mm and a disc area of 22·0 cm^2 or equivalent outer circular radius of 2·64 cm. On the basis of the measurements of Perey (1957), Nachemson (1960), Eie (1966) and Farfan *et al.* (1970), who determined that the nucleus occupies approximately 25–50 per cent of the disc's cross-section area, the outer radius of the nucleus pulposus, r_n, was taken to be 0·707 times the outer radius of the disc. The vertebral body heights for the *L2/L3* level were taken to be equal to 2·8 cm, which was the average of the anterior and posterior mean vertebral heights reported by Lanier (1939).

The coarse mesh model is similar to the fine mesh with the following exceptions: (a) regions 2 and 3 are treated as soft bone; (b) only a portion of the vertebral body is modelled (i.e. the body height was truncated); and (c) fewer finite elements are used. This mesh was used for the various parameter studies to save computer time. Table 1 lists the pertinent dimensions used with the coarse mesh.

A standard axisymmetric linear finite element technique (Wilson, 1965) with triangular, linear displacement elements was used. The incompressible, hydrostatic nucleus was incorporated by a technique developed by Belytschko and Kulak (1972), which requires only a single layer of elements in the incompressible material. The other portions of the model were assumed to be compressible.

MATERIAL PROPERTIES OF ANNULUS

Since the annulus fibrosis consists of approximately equal parts of fibers oriented at $+\phi$ and $-\phi$ (Fig. 3), it is orthotropic with respect to the vertical, radial and circumferential coordinates. Furthermore, each lamella is orthotropic in its plane with respect to coordinates normal and tangent to the fiber direction. The stress–strain law in an axisymmetric solid for a linear, orthotropic material is given by

$$\begin{Bmatrix} \sigma_\theta \\ \sigma_z \\ \sigma_r \\ \sigma_{rz} \end{Bmatrix} = \begin{bmatrix} C_{11} & C_{12} & C_{13} & 0 \\ C_{12} & C_{22} & C_{23} & 0 \\ C_{13} & C_{23} & C_{33} & 0 \\ 0 & 0 & 0 & G_{rz} \end{bmatrix} \begin{Bmatrix} \epsilon_\theta \\ \epsilon_z \\ \epsilon_r \\ \epsilon_{rz} \end{Bmatrix} \tag{2}$$

This stress–strain law contains seven distinct constants. For the purpose of relating these constants to Galante's experimental results on tensile specimens, consider the stress–strain relation for a single lamella in a state of plane stress in a $(\bar{x}_1, \bar{x}_2)$ coordinate system shown in Fig. 3. Here $\bar{x}_1$ is in the fiber direction, $\bar{x}_2$ is normal to $\bar{x}_1$ and in the plane of the lamella. Since the lamella is orthotropic with respect to the $(\bar{x}_1, \bar{x}_2)$ coordinates (see, Jayne and Suddarth e.g., 1965),

$$\begin{Bmatrix} \tilde{\sigma}_1 \\ \tilde{\sigma}_2 \\ \tilde{\sigma}_{12} \end{Bmatrix} = \begin{bmatrix} E_L/\kappa & \nu_{LT}E_L/\kappa & 0 \\ \nu_{LT}E_L/\kappa & E_T/\kappa & 0 \\ 0 & 0 & G_{LT} \end{bmatrix} \begin{Bmatrix} \tilde{\epsilon}_1 \\ \tilde{\epsilon}_2 \\ \tilde{\epsilon}_{12} \end{Bmatrix} \tag{3}$$

where

$$\kappa = 1 - \nu_{LT}\nu_{TL}$$
$$\nu_{LT}E_L = \nu_{TL}E_T. \tag{4}$$

Here E_L and E_T are the longitudinal and transverse Young's moduli, ν_{LT} and ν_{TL} the Poisson's ratios and G_{LT} the shear modulus. Let the stress–strain matrix in equation (3) be denoted by $[\tilde{C}]$. By means of tensor transformations, the stress–strain matrix $[\hat{C}(\alpha)]$ in a

Table 1. Vertebra and disc dimensions

Vertebra level	Vertebral body height (cm)	Truncated body height (cm)	Disc level	Disc circular radius (cm)	Disc height (cm)
L3	2·80	0·350	*L2/L3*	2·13	1·14
L2	2·79	0·349	*T12/L1*	1·99	0·84
L1	2·72	0·339	*T10/T11*	1·81	0·51
T12	2·57	0·320	*T8/T9*	1·64	0·45
T11	2·43	0·304			
T10	2·30	0·288			
T9	2·14	0·267			
T8	2·07	0·258			

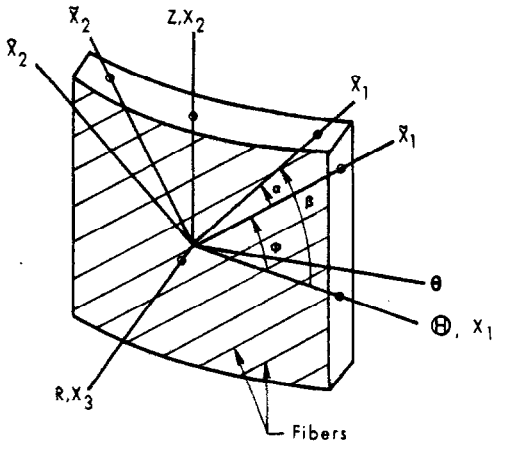

Fig. 3. Coordinate systems.

coordinate system $(\hat{x}_1, \hat{x}_2)$ rotated from $(\tilde{x}_1, \tilde{x}_2)$ by α is given by

$$[\hat{C}(\alpha)] = [\lambda]^T [\tilde{C}] [\lambda] \tag{5}$$

where

$$[\lambda] = \begin{bmatrix} c^2 & s^2 & -cs \\ s^2 & c^2 & cs \\ 2cs & -2cs & c^2 - s^2 \end{bmatrix} \quad \begin{matrix} c = \cos\alpha \\ s = \sin\alpha. \end{matrix} \tag{6}$$

The stress–strain matrix for a macroscopic sample with respect to the $(\bar{x}_1, \bar{x}_2)$ axes is obtained by averaging the stress–strain laws of the two distinct types of lamellae, which gives

$$\begin{Bmatrix} \hat{\sigma}_1 \\ \hat{\sigma}_2 \\ \hat{\sigma}_{12} \end{Bmatrix} = [\bar{C}] \begin{Bmatrix} \hat{\epsilon}_1 \\ \hat{\epsilon}_2 \\ 2\hat{\epsilon}_{12} \end{Bmatrix} = \tfrac{1}{2}[\hat{C}(\beta - \phi)] + [\hat{C}(\beta + \phi)]\{\hat{\epsilon}\}. \tag{7}$$

It should be noted that at an arbitrary angle of inclination β other than zero or 90°, the stress–strain law is not orthotropic, and hence shear strains and normal stresses are coupled. This results in nonzero values of $\bar{C}_{13}$ in equation (7).

In the tensile specimen, the state of stress is uniaxial so σ_2 and σ_{12} vanish. By imposing these conditions on equation (7) we find

$$\hat{\sigma}_1 = Q(\beta)\hat{\epsilon}_1 \tag{8}$$

where

$$Q_{11}(\beta) = \frac{\hat{C}_{11}\hat{C}_{22}\hat{C}_{33} + 2\hat{C}_{12}\hat{C}_{13}\hat{C}_{23} - \hat{C}_{22}\hat{C}_{13}^2 - \hat{C}_{33}\hat{C}_{12}^2 - \hat{C}_{11}C_{23}^2}{\hat{C}_{22}\hat{C}_{33} - \hat{C}_{23}^2}. \tag{9}$$

The values of the compliance, $1/Q(\beta)$, as measured at various values β_i by Galante are shown in Fig. 4. In order to find values of the elastic constants E_L, E_T, ν_{LT} and G_{LT} to best match Galante's experimental results, a least square procedure was used. For each trial value of the elastic constants, $[\hat{C}(\beta_i)]$ and hence $Q(\beta_i)$ were found by equations (2, 5, 7 and 9) for each angle β_i at which the tensile properties were measured. By minimizing

$$f = \sum_{i=1}^{6} [Q(\beta_i) - Q^{\text{exp}}(\beta_i)]^2 \tag{10}$$

the values of the elastic constants that best match the experimental results were obtained. These values are given in Table 2.

The compliance function, $1/Q(\beta)$, associated with these elastic constants is also shown in Fig. 4. Though it has the principal feature of the experimental results, the discrepancies are quite large at certain angles. Probable causes are: (1) the material is nonlinear and therefore cannot accurately be represented by linear relationships rotated into different angles; (2) in tensile specimens, at certain angles most of the fibers are cut, so if the fiber bond strength is low, considerable separation of fibers may occur and so underestimate the stiffness of the intact material.

Another difficulty in ascertaining material properties from tensile tests is caused by the insensitivity of tensile behavior to Poisson's ratio ν_{LT} and the shear modulus G_{LT}. This is illustrated in Fig. 5, where $1/Q(\beta)$ is shown for various values of these parameters. As can be seen from this figure, even large variations in these material parameters produce only small alterations in the tensile properties at various angles. Hence, these material parameters are very difficult to determine from tensile tests and so they were here established by parameter studies in conjunction with overall properties of the disc as described in the following section.

The constants C_{ij} in equation (2) are obtained from the material constants E_L, E_T, ν_{LT} and G_{LT} as follows. Consider again a single lamella in the coordinate system $(\tilde{x}_1, \tilde{x}_2, \tilde{x}_3)$ as shown in Fig. 3, with $\tilde{x}_1$ in the fiber direction, $\tilde{x}_2$ normal to it and $\tilde{x}_3$ in the radial direction.

Table 2. Material properties of annulus

	E_L (kp/mm^2)	E_T (kp/mm^2)	G_{LT} (kp/mm^2)	ν
Fit to Galante	0·540	0·033	0·217	0·42
Fit to Rolander at				
11 kp	3·60	0·090	0·060	0·45
26 kp	5·00	0·125	0·084	0·45
44 kp	6·60	0·165	0·110	0·45
70 kp	8·30	0·207	0·138	0·45
Assumed degenerate disc	0·18	0·090	0·060	0·45

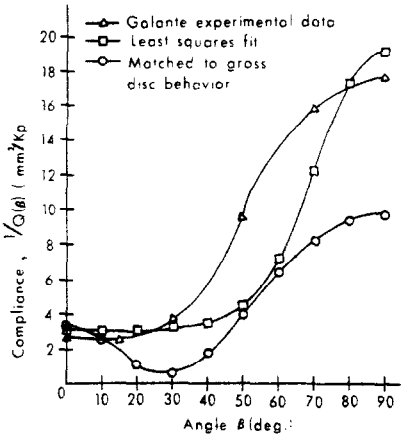

Fig. 4. Comparison of experimental values of annulus fibrosus compliance with those based on material properties as determined by: (a) least squares fit; and (b) matching of gross disc behavior.

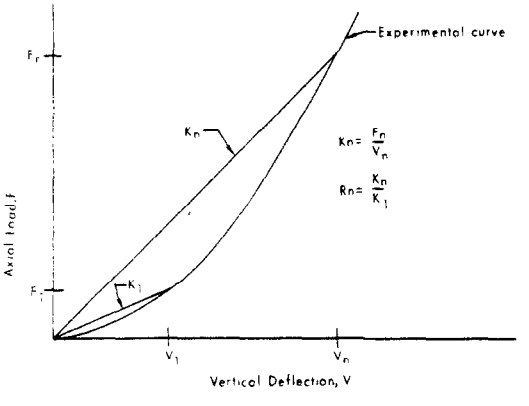

Fig. 5. Geometric construction used for secant ratio method.

According to Jayne and Suddarth (1965),

$$\bar{C}_{11} = \frac{\tilde{E}_1}{D}(1 - \tilde{\nu}_{32}\tilde{\nu}_{23}) \qquad \bar{C}_{22} = \frac{E_2}{D}(1 - \tilde{\nu}_{13}\tilde{\nu}_{31})$$

$$\bar{C}_{12} = \frac{\tilde{E}_1}{D}(\tilde{\nu}_{12} + \tilde{\nu}_{32}\tilde{\nu}_{13}) \qquad \bar{C}_{23} = \frac{E_2}{D}(\tilde{\nu}_{23} + \tilde{\nu}_{13}\tilde{\nu}_{21})$$

$$\bar{C}_{13} = \frac{\tilde{E}_1}{D}(\tilde{\nu}_{13} + \tilde{\nu}_{12}\tilde{\nu}_{23}) \qquad \bar{C}_{33} = \frac{E_3}{D}(1 - \tilde{\nu}_{12}\tilde{\nu}_{21})$$

$$\bar{C}_{44} = G_{13}. \tag{11}$$

By definition

$$D = 1 - 2\nu_{12}\nu_{23}\nu_{31} - \nu_{13}\nu_{31} - \nu_{12}\nu_{21} - \nu_{23}\nu_{32}$$

$$\tilde{E}_1 = E_1 \qquad \tilde{E}_2 = E_T \qquad \nu_{12} = \nu_{LT}. \tag{12}$$

If we now assume that each lamella is transversely isotropic, it follows that

$$\tilde{E}_3 = \tilde{E}_2 = E_T \qquad \tilde{\nu}_{12} = \tilde{\nu}_{13} = \nu_{LT} \tag{13}$$

$$\bar{G}_{13} = \bar{G}_{12} = G_{LT} \qquad \bar{G}_{23} = \frac{E_2}{2(1 + \nu_{23})}. \tag{14}$$

From the assumption that the material is compressible, it follows that

$$\tilde{\nu}_{23} \leq 1 - \tilde{\nu}_{13} \tag{15}$$

with the equality corresponding to incompressibility. The remaining Poisson ratios are found by

$$\tilde{\nu}_{ij}\tilde{E}_j = \tilde{\nu}_{ji}\tilde{E}_i \qquad \text{(no sum)}.$$

The stress–strain matrix $[C]$ in the (r, z, θ), i.e. (x_1, x_2, x_3) coordinates, as shown in equation (2) is then found by the tensor transformation and averaging the material constants in the two orientations.

In order to gain insight into the nonlinear behavior of the disc, a secant ratio method was employed to determine material constants for various load levels. The procedure was as follows. The secant stiffness, K_n,

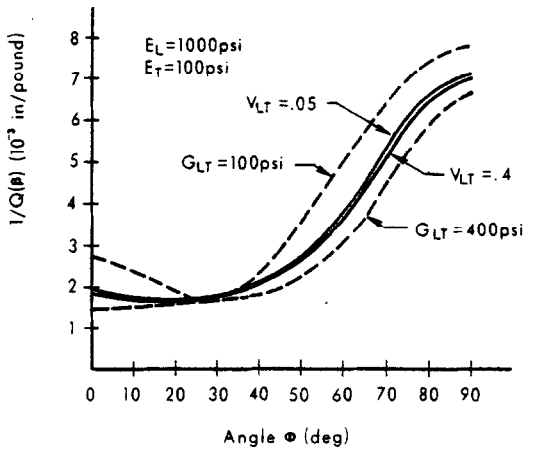

Fig. 6. Effect of Poisson's ratio, v_{LT}, and shear modulus, G_{LT}, on compliance.

at various load levels was computed from an experimental load deflection curve for the *L2/L3* disc (Fig. 5). Next, the ratio, R_n, between the secant stiffness at load level F_n and the secant stiffness at a reference load, F_1, was computed. The Young's moduli and shear moduli at load F_n were then obtained by multiplying the moduli at the reference load level, F_1, by the ratio R_n. Poisson's ratios remained unchanged.

RESULTS*

The model was employed for studying the behavior of the disc under compressive axial loading and the influence of material parameters and geometric variations associated with disc levels in the thoracolumbar spine. The load was applied by prescribing a uniform vertical displacement at the top surface of the model; the bottom surface was fixed. The total axial load resulting from these stresses divided by the area of the disc–body interface is designated by p_a, the applied pressure as defined by Rolander. Since Rolander's results show somewhat nonlinear behavior, a loading of 11 kp was chosen as a reference point.

The orthotropic material constants of the annulus fibrosis were derived by adjusting the material constants obtained from Galante's results so as to match the overall disc behavior measured by Rolander. The material constants obtained are listed in Table 2, and the compliance, $1/Q(\beta)$, is plotted for these values in Fig. 4.

A comparison between the finite element results obtained with these material properties and Rolander's experimental results on the macroscopic behavior of the disc is given in Table 3. The agreement of the computed and measured gross behavior of the disc is excellent. The computed ratio between the internal pressure and the applied pressure, p_i/p_a, is 1·4, which is in the range of 1·3–1·5 measured by Nachemson. The annular material was assumed to be compressible. Kobayashi *et al.* also used a slightly compressible material to represent the incompressible tissue of the corneo–scleral shell of the eye and found that the effects of this assumption are slight.

The matching was accomplished through a series of parameter studies which will not be described in detail. However, two findings of this study are of interest: (1) the gross behavior of the disc cannot be matched by an isotropic annulus; if the annulus is assumed isotropic, the intradiscal pressure is about 1·1 p_a and the bulge to compression ratio does not match experimental results; (2) the behavior predicted on the basis of Galante's measurements differs significantly with experimental findings. The curve of the compliance, $1/Q(\beta)$, (Fig. 4) corresponding to the matched material constants is stiffer at large angles than Galante's experimental results. This may indicate that the cutting of fibers to obtain a tensile specimen probably causes a large reduction in strength.

The normal stress distributions through the thickness of the annulus at the two levels indicated in Fig. 2 are shown in Fig. 7. The maximum tangential stress $\sigma_{\theta\theta}$ occurs along the outer periphery and its value is 3·35 p_a. Nachemson, by using a hoop analysis, predicted a maximum stress between 3 p_a and 5 p_a. The axial stress, σ_{zz}, is compressive at the inner radius of

* A portion of this study was published earlier as ASME Paper 72-WA/BHF-12. That paper contained some numerical errors which have since been corrected.

Table 3. Comparison of experimental and finite element results (11 kp load)

	Applied pressure p_a (kp/cm²)	Disc bulge (mm)	Disc compression (mm)	Nucleus pressure, P_i (kp/cm²)
Finite element	0·53	0·61	0·23	0·71
Rolander	0·50	0·60	0·22	0·75*
Per cent difference	6·00	1·67	4·50	5·30

* Based on Nachemson's experimental relationship: $p_i = 1{\cdot}5\ p_a$.

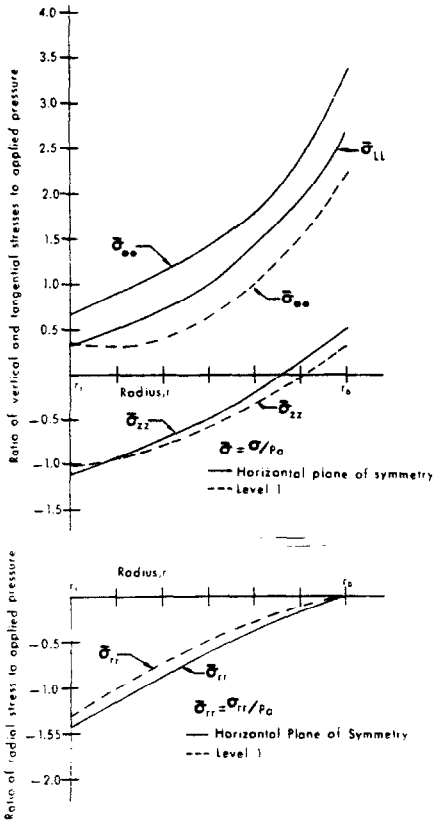

Fig. 7. Stress distribution in a normal disc.

the annulus, while at the outer radius it becomes tensile. It appears that in normal discs a large part of the axial load is transmitted through the nucleus. The radial stress distribution is similar to that obtained by Sonnerup's semi-analytic model. The normal stress in the fiber direction, σ_{LL}, is also shown. It can be seen that except for a small region at the inner radius, the fiber stresses are tensile when the annulus is compressed.

In order to study the effects of changes in material properties associated with disc degeneration, the effect of the longitudinal Young's modulus, E_L, on the overall behavior of the disc was investigated. The results are shown in Fig. 8. Aging of collagen tissue is associated with loss of elasticity, i.e. increase in elastic modulus. On the other hand, as reported by Farfan *et al.* (1972), disc degeneration is also characterized by radial annular tears, which corresponds to a decrease in effective modulus. From the results obtained, it is apparent that the latter phenomenon is predominant: reduction of the elastic modulus results in lower intradiscal pressure and greater compression and bulging, which corresponds with the changes observed in degenerated discs by Hirsch and Nachemson and by Brown *et al.* (1957). Increasing the elastic modulus increases the intradiscal pressure and annular stresses, though the changes are smaller than those caused by annular tears. It should be noted that these results neglect the degenerative changes of the nucleus.

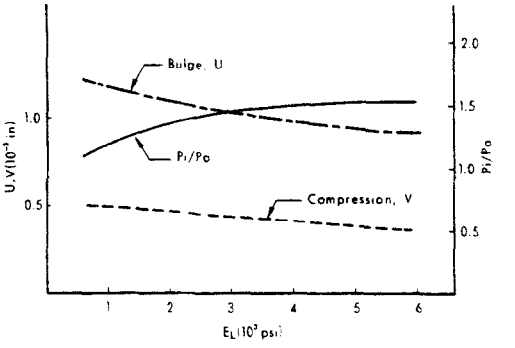

Fig. 8. Effect of longitudinal modulus, E_L, on disc bulge, disc compression, and nucleus pressure.

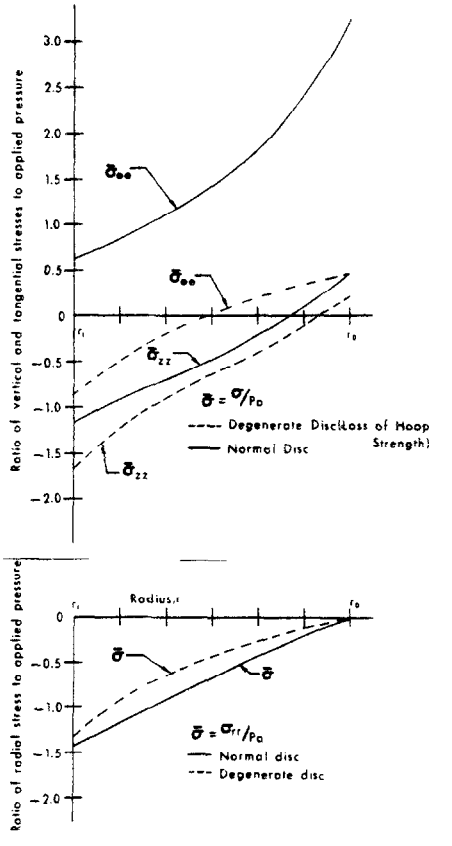

Fig. 9. Stresses in a normal and in a degenerate disc.

The stress distributions for a disc with decreased elastic modulus, i.e. a disc that may be termed degenerate, is shown in Fig. 9. The elastic constants used to obtain the results are given in Table 2; these values were picked arbitrarily so the results only have qualitative significance. It can be seen that these changes result in a considerable reduction in hoop stress and an increase in the compressive axial stress. Evidently, in a disc with a degenerate annulus, a large part of the axial load is carried by the annulus.

The effect of size and shape variations on the axial stiffness of the thoracolumbar discs was investigated by varying the model dimensions as given in Table 1. The dimensions used for the vertebral body heights at each level are the averages of the anterior and posterior body heights reported by Lanier. The disc heights which are measured at the outer periphery as shown in Fig. 2, are those estimated by Schultz *et al.* (1973), while the disc's circular radius was taken to be equal to one-half of the sum of the frontal and sagittal plane vertebral diameters as reported by Lanier. It was assumed that neither material properties nor the ratio of the inner to outer radii of the annulus vary with disc level.

The results of this study are shown in Fig. 10 along with maximum and minimum secant stiffnesses based on the experimental static axial load deflection curves

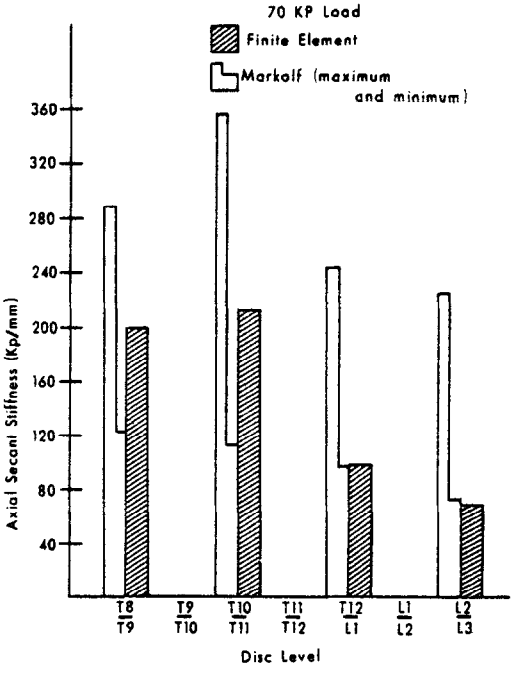

Fig. 10. Variation of axial disc stiffness with disc level.

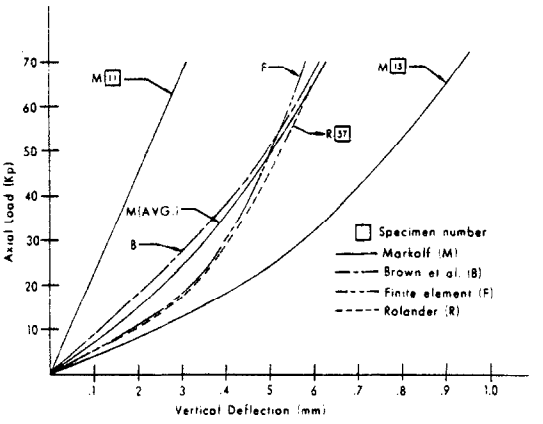

Fig. 11. Load deflection curves for an *L2/L3* disc.

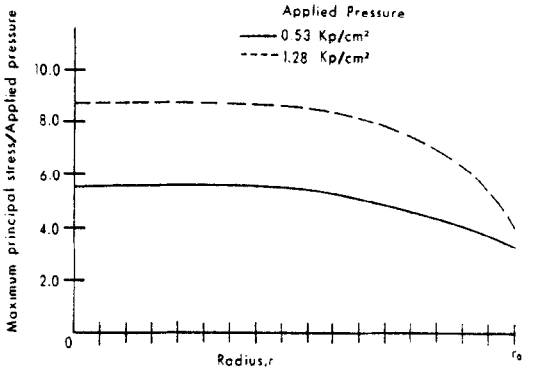

Fig. 12. Principal stress distribution in the bony end plate.

of Markolf. Both the computed and experimental stiffnesses are at a load of 70 kp. The computed axial stiffnesses of the thoracolumbar disc are in reasonable agreement with Markolf's experimental results, though Markolf's stiffnesses are somewhat higher at the *T12/L1* and *L2/L3* levels. The difference between the two may be caused by the effects of the anterior and posterior longitudinal ligaments, which were not cut away in Markolf's tests, or nonlinear behavior.

Figure 11 shows the nonlinear load deflection curve obtained by using the secant ratio method previously described, along with the experimental curves of Rolander, Markolf and Brown *et al.* The computed values are based on Rolander's secant stiffness with the reference stiffness, K_n, taken at 11 kp. The material constants used at these load levels are given in Table 1. The computed bulge, though not reported here, was compared to the bulge measured by Rolander and agrees within 8 per cent or less. Similarly, the computed nucleus pressures agree with experimental findings. Hence, the material constants obtained here

appear to yield a model whose behavior corresponds well with available experimental results.

The ratio of the maximum principal stress to the applied pressure in the bony end plate is shown in Fig. 12. The principal stress remained fairly constant in the central portion of the plate and decreased near the outer portion. These results may be of value in predicting the disc load level at which an endplate fracture will occur. The maximum principal stress/applied pressure ratio increased as the applied pressure increased.

CONCLUSION

The present study illustrates the usefulness of the finite element model in estimating the material properties of the disc and predicting the mechanical behavior of the components within the disc unit. Good correlation is found between the model behavior and experimental studies. The model provides detailed information on the axisymmetric stress distribution within the disc unit, the hydrostatic pressure in the nucleus pulposus, and the deformations of the annulus and vertebral body. The model also permits the study of degenerative changes and illustrates the nonlinear behavior of the disc unit. The present studies neglected deviations from rotational symmetry. However, in compressive axial loading, the asymmetry of the disc should have little effect on stress distributions and overall behavior.

It was found that:

1. The overall mechanical behavior of the disc cannot be adequately represented by isotropic material behavior;
2. Material properties of the annulus obtained by direct tensile test measurements underestimate the stiffness;
3. Reasonable predictions of variations of disc stiffness with vertebral level can be made on the basis of geometry.

Acknowledgements—This research was supported in part by Public Health Service Grant AM 15575 and Social and Rehabilitation Service Grant 23P55785.

REFERENCES

Beadle, O. A. (1931) The intervertebral discs. Observations on their normal and morbid anatomy in relation to certain spinal deformities. Medical Research Council. Special report series. His Majesty's Stationery Office, London. No. 161.

Belytschko, T. and Kulak, R. F. (1972) A finite element method for a solid enclosing an inviscid, incompressible fluid. *J. Appl. Mech. 40 Trans. ASME* **95**, 609–610.

Brown, T., Hansen, R. J. and Yorra, A. J. (1957) Some mechanical tests on the lumbosacral spine with particular reference to the invertebral disc. *J. Bone Jt Surg.*, **39A**, 1135–1164.

Eie, N. (1966) Load capacity of the low back. *J. Oslo City Hospital* **16**, 75–98.

Evans, F. G. (1970) Mechanical properties and histological structure of human cortical bone. ASME publication 70-WA/BHF-7.

Farfan, H. F., Cossette, J. W., Robertson, G. H., Wells, R. V. and Kraus, H. (1970) The effects of torsion on the lumbar intervertebral joints: the role of torsion in the production of disc degeneration. *J. Bone Jnt Surg.* **52-A**, 468–494.

Fick, R. (1904–1911) *Handbuch der Anatomie und Mechanik der Gelenke unter Berucksichtigung der bewegenden Muskeln*. Fischer, Jena.

Galante, J. O. (1967) Tensile properties of the human lumbar annulus fibrosus. *Acta Orthop. Scand. Suppl.* **100**.

Hirsch, C. and Nachemson, A. (1954) New observations on the mechanical behavior of lumbar disc. *Acta Orthop. Scand.* **23**, 254–283.

Horton, W. G. (1958) Further observations in the elastic mechanism of the intervertebral disc. *J. Bone, Jnt Surg.* **40-B**, 552–557.

Jayne, B. A. and Suddarth, S. K. (1965) Orientation effects in the mechanical behavior of anisotropic structural materials. ASTM Special Technical Publication No. 405.

Kobayashi, A. S., Woo, S. L. Y., Lawrence, C. and Schlegel, W. A. (1971) Analysis of the corneoscleral shell by the methods of direct stiffness. *J. Biomechanics* **4**, 323–330.

Lanier, Jr., R. R. (1939) The presacral vertebrae of American White and Negro males. *Amer. J. Phys. Anthrop.* **25**(3), 341–420.

Markolf, K. L. (1971) Engineering characteristics of the human intervertebral joint. Ph.D. Thesis, University of California.

Markolf, K. L. (1972) Deformation of the thoracolumbar intervertebral joints in response to external loads. *J. Bone Jnt Surg.* **54-A**, 511–533.

Nachemson, A. (1960) Lumbar intradiscal pressure. *Acta Orthop. Scand., Suppl.* **43**.

Perey, O. (1957) Fracture of the vertebral end-plate in the lumbar spine. An experimental biomechanical investigation. *Acta Orthop. Scand. Suppl.* **25**.

Rolander, S. D. (1966) Motion of the lumbar spine with special reference to the stabilizing effect of posterior fusion. Thesis. *Acta Orthop. Scand. Suppl.* 90.

Rouviere, H. (1921) Sur la texture des disques intervertebraux. *C. R. Soc. Biol.* **85**, 156–157.

Schultz, A. B., Belytschko, T. B., Andriacchi, T. P. and Galante, J. O. (1973) Analog studies of forces in the human spine: mechanical properties and motion segment behavior. *J. Biomechanics* **6**, 373–383.

Sonnerup, L. (1972) A semi-experimental stress analysis of the human intervertebral disc in compression. *Exp. Mech.* **12**(3), 142–127.

Wiederhielm, C. A., Kobayashi, A. S., Stromberg, D. D. and Woo, S. L. Y. (1968) Structural response of relaxed and constricted arterioles. *J. Biomechanics* **1**, 259–270.

Wilson, E. L. (1965) Structural analysis of axisymmetric solids. *AIAA J.* **3**(12), 2269–2274.

Yamada, H. (1970) *Strength of Biological Materials*. Williams and Wilkins, Baltimore.